

CFD Analysis of Container Ship Manoeuvring Performance under Different Trim Conditions

Haechan Yun¹, Wooseok Choi¹, Gyeongseo Min¹, Younguk Do¹, Kangmin Kim¹, Daejeong Kim²,
Saishuai Dai³, Tahsin Tezdogan⁴, Soonseok Song^{1*}

*corresponding author email: s.song@inha.ac.kr

¹Department of Naval Architecture & Ocean Engineering, Inha University, Republic of Korea

²Division of Navigation Convergence Studies, Korea Maritime & Ocean University, Republic of Korea

³Department of Naval Architecture, Ocean and Marine Engineering, University of Strathclyde, United Kingdom

⁴Department of Civil, Maritime and Environmental Engineering, University of Southampton, United Kingdom

Abstract

Containerships often operate under various trim conditions, where the ship's bow or stern is inclined due to differing loading conditions. These trim conditions can significantly affect not only the ship's resistance and propulsion performances but also its manoeuvrability. This study investigates the impact of trim variations on the manoeuvring performance of the KRISO Container Ship (KCS) using Computational Fluid Dynamics (CFD). Free-running CFD simulations were performed under different trim conditions, ranging from -3° to $+2^\circ$. The results demonstrate how trim conditions influence the turning and zigzag manoeuvre characteristics of the vessel, highlighting their impact on ship manoeuvrability.

Keywords: ship manoeuvrability; Computational Fluid Dynamics (CFD); turning circle test; zigzag test

1 Introduction

Modern vessels are increasingly larger to meet global trade demands. This presents new challenges in navigating through congested waterways and ports. Poor manoeuvrability can result in collisions, groundings, and environmental damage. Therefore, comprehensive evaluation of ship handling characteristics is critical for maritime safety. Among the various factors affecting ship manoeuvrability, the trim condition plays a significant role, as it directly influences the distribution of hydrodynamic forces acting on the hull. This influence is particularly pronounced in container ships, where variations in container weight and type can cause frequent trim changes. As such, trim has a direct effect on fuel consumption and greenhouse gas emissions, prompting several studies to explore its effects on resistance and self-propulsion performance (e.g., Park et al., 2013; Seo et al., 2015; Han et al., 2015; Le et al., 2021; Sherbaz et al., 2014). Under ship trim conditions, the point where resistance is minimized varies depending on the ship's speed and hull form, but based on the results of previous studies, it can be confirmed that minimum resistance occurs near the even keel condition. While optimizing resistance and propulsion is important, it does not necessarily ensure optimal manoeuvrability (Carrica et al., 2016). Therefore, the precise evaluation of a vessel's manoeuvring performance under various trim conditions is of critical

importance. This is because manoeuvrability is governed by a complex interplay of hydrodynamic forces that are themselves sensitive to trim variations. As such, more advanced and refined analytical methods are required to accurately capture these effects.

To address this need for accurate manoeuvring analysis, Computational Fluid Dynamics (CFD) has emerged as a powerful tool with the increase in computing power. CFD research has become more common in the field of naval architecture, offering the advantage of accurately analysing the viscous and free surface effects that are crucial for understanding ship behaviour under different operating conditions. Numerous studies on ship resistance and self-propulsion have been conducted using CFD (e.g., Carrica et al., 2010; Castro et al., 2011; Song et al., 2024b; Lee et al., 2021; He et al., 2022; Huang et al., 2022; Mikulec et al., 2023). Furthermore, CFD studies on ship manoeuvrability have been advancing and increasing in recent years. Carrica et al. (2015) evaluated the manoeuvring performance of the KRISO Container Ship (KCS). The zigzag manoeuvre simulations showed good agreement with experimental data, demonstrating that CFD-based evaluation of ship manoeuvrability is valid. Song et al. (2024a) measured the changes in manoeuvrability with respect to GM variation. The results were found to be consistent with the trends observed in the experimental study by Yun et al. (2020). These studies demonstrated that CFD provides a reliable method for evaluating ship manoeuvrability. The approach offers advantages in terms of cost and flexibility compared to experimental testing.

Despite this, research on ship manoeuvrability under trim conditions remains limited. Recently, several studies have begun addressing this topic (e.g., Himaya et al., 2022; Yun et al., 2020). Yun et al. (2020) investigated the effect of changing the centre of gravity of the KCS in three directions, effectively implementing variations in trim, heel, and GM, and demonstrated how these changes influence the ship's manoeuvrability through experimental testing. Similarly, Himaya et al. (2022) developed an MMG model through experiments and CFD to assess ship manoeuvrability under various trim and draft conditions. While these studies have made important contributions, experimental approaches require significant resources and testing facilities, and MMG based methods may not capture the fully dynamic interactions between the hull and free surfaces. Therefore, research on fully coupled 6-degree-of-freedom (6-DoF) manoeuvrability under trim conditions using CFD remains an area for further development.

The present study aims to investigate ship manoeuvrability under various trim conditions using the KRISO Container Ship (KCS). To achieve this, free-running CFD simulations were conducted under various trim conditions. The dynamic overset grid was employed to simulate the motion of the ship and rudder, and the body-force propeller method was used to represent the propeller's effects instead of using a rigid body model.

2 Methodology

2.1 Governing equation

The present study employs a computational fluid dynamics (CFD) approach to analyse turbulent free-surface flows using the Unsteady Reynolds-Averaged Navier-Stokes (URANS) equations. The numerical simulations were carried out with the commercial CFD solver STAR-CCM+.(version 19.04.009)

The governing equations for incompressible flow are formulated as:

$$\frac{\partial u_i}{\partial x_i} = 0 \quad (1)$$

$$\frac{\partial u_i}{\partial t} + \rho \frac{\partial (u_j u_i)}{\partial x_j} = -\frac{\partial P}{\partial x_i} + \frac{\partial}{\partial x_j} \left(\mu \frac{\partial u_i}{\partial x_j} \right) - \rho \frac{\partial (\overline{u'_i u'_j})}{\partial x_j} \quad (2)$$

where ρ represents fluid density, u_i is the time-averaged velocity component, P denotes pressure, and μ is the dynamic viscosity. The Reynolds stress term $\overline{u'_i u'_j}$ accounts for the effects of turbulence.

.Spatial discretization of the computational domain utilized the Finite Volume Method (FVM). Effective pressure–velocity coupling was achieved through implementation of the Semi-Implicit Method for Pressure-Linked Equations (SIMPLE) algorithm. Turbulence effects were modelled using the Shear Stress Transport (SST) $k-\omega$ formulation, which offers enhanced accuracy in regions dominated by high shear rates and adverse pressure gradients. The air-water interface was resolved using the Volume of Fluid (VOF) technique.

2.2 Hull Geometry

In this study, the KCS hull form provided by KRISO was used with a scale ratio of 37.89, and detailed ship information is shown in Table 1. The geometry of the KCS model can be found in Fig. 1. The Radius of gyration for yaw (K_{ZZ}/l_{wl}) of the original vessel is 0.25, but since validation was conducted using experimental data from SIMMAN 2020, the given value of 0.258 was adopted instead.



Fig. 1. Geometry of KCS

Table 1 Principal particulars of full-scale and model-scale KCS

		Full-scale	Model-scale
Scale factor	λ	1	37.89
Length of waterline	L_{WL} (m)	232.5	6.136
Beam at waterline	B_{WL} (m)	32.2	0.850
Depth	D (m)	19	0.501
Design draft	T (m)	10.8	0.285
Displacement volume	∇ (m ³)	52030	0.9565
Wetted surface area (w/o rudder)	S (m ²)	9530	6.6381
Block coefficient	C_B	0.651	0.651
Longitudinal centre of buoyancy	LCB (%), fwd+	-1.48	-1.48
Metacentric height	M (m)	0.6	0.016
Radius of gyration for roll	k_{xx}/B	0.4	0.4
Radius of gyration for pitch & yaw	$k_{yy}/L_{wl}, k_{zz}/L_{wl}$	0.25	0.258
Max. rudder turn rate	$\dot{\delta}_{max}$ (°/s)	2.32	14.28








2.3 Trim conditions

The numerical analysis comprises seven trim scenarios: three trim-by-bow conditions, three trim-by-stern conditions, and one even-keel configuration. For both trim-by-bow and trim-by-stern cases, two scenarios correspond to small trim angles (0.25° and 0.5°), while the third represents a large trim angle. The longitudinal centre of gravity (LCG) positions and the metacentric height (GM) values for each trim angle are presented in Table 2, where the GM values were determined through heel tests.

Although such a large trim angle is rarely encountered in actual ship operations, it was included to examine the general trend in manoeuvring performance. Additionally, for large trim angles in both trim-by-bow and trim-by-stern conditions, the vessel exhibits abnormal motion characteristics that make manoeuvring tests difficult to conduct. Therefore, the maximum feasible angles for manoeuvring operations were selected: 2° trim-by-bow and 3° trim-by-stern

For clarity and intuitive understanding, the terms “Bow-down” and “Stern-down” are used together with general terms “trim-by-bow” and “trim-by-stern,” respectively.

Table 2 Numerical simulation cases and corresponding variation in longitudinal centre of gravity of the model ship (in model-scale)

Trim Conditions	Trim angle (deg)	LCB (%), fwd+	GM (m)	
Trim-by-stern (Stern-down)	-3.00	-1.522	0.045	
	-0.50	-1.487	0.024	
	-0.25	-1.484	0.020	
Evenkeel	0	-1.480	0.016	
Trim-by-bow (Bow-down)	0.25	-1.476	0.013	
	0.5	-1.473	0.010	
	2	-1.452	0.0016	

2.4 boundary conditions

The numerical setup is illustrated in Fig. 2., where the background domain moves with the KCS vessel, allowing motion in sway, surge, and yaw directions. The overset grid, including the KCS, is modelled with 6-degree-of-freedom (6-DoF), while the rudder overset is constrained within the ship's coordinate system, moving together with the vessel.

The boundary conditions of the domain were set with a pressure outlet at the top surface and velocity inlets on the remaining five surfaces for the simulation.

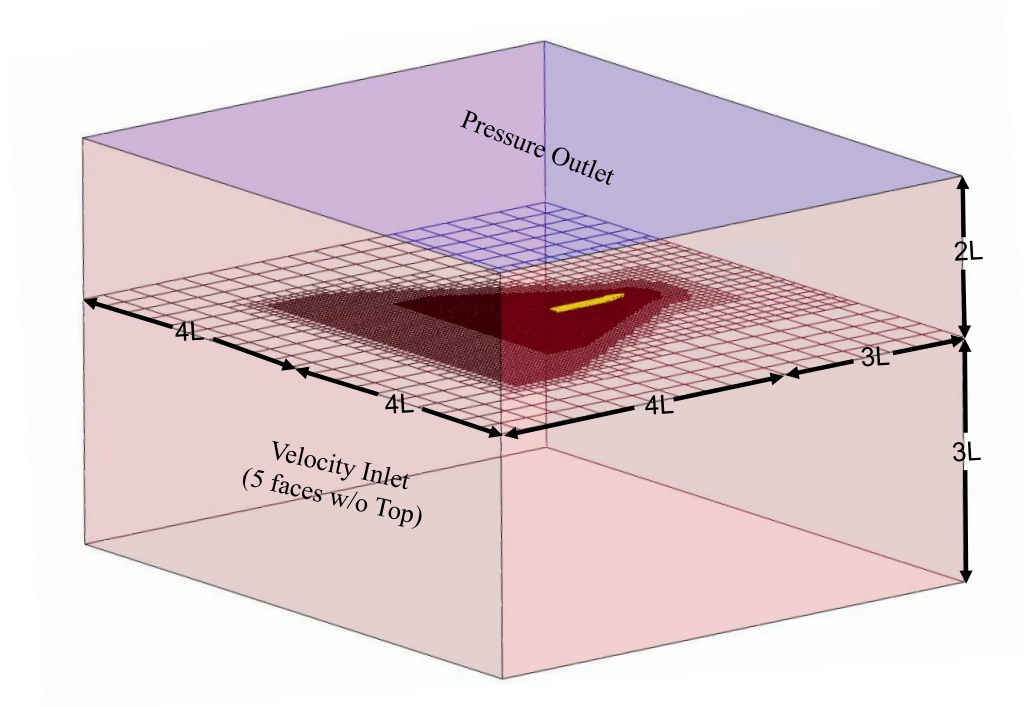


Fig. 2. Domain Boundary conditions

2.5 Body-force propeller method

This study implemented propeller forces through the body-force method, avoiding the computational complexity of modelling the rotating propeller geometry directly. The body-force propeller method has been validated in the field of ship manoeuvring prediction (Kim et al., 2021a; Kim et al., 2025; Araki et al., 2021; Li et al., 2022). According to Jiang et al. (2025), this approach can reduce computational time by up to 35-fold compared to simulations involving the actual rotation of the propeller disk, while still effectively representing thrust and moment. Therefore, considering computational efficiency, the body force method was adopted in the present work. Although the standard propeller for the KCS hull is the KP505, MARIN's free-running experimental employed a modified 5533R propeller configuration. Thus, the propeller force implementation in this study was based on the POW test of the 5533R propeller to ensure proper validation against the experimental data.

2.6 Mesh generation

The mesh was generated using the built-in mesher of STAR-CCM+. A dynamic overset grid was applied to capture the motion of the ship and rudder. To ensure accuracy in the overlapping regions of the overset grid, the mesh size was designed to closely match that of the surrounding regions. Additionally, mesh refinements were applied around the rudder and in the wake region to accurately capture the highly variable flow near the rudder and to properly simulate the Kelvin wake generated by the ship. These refinements in the wake region, particularly those for resolving the Kelvin wake, can be observed in the mesh refinement view shown in Fig. 3. The target wall y^+ was set to 40 and was represented using a prism layer. The prism layer thickness was adjusted so that the cell size gradually increased, allowing a smooth transition to the outer mesh and improving computational accuracy.

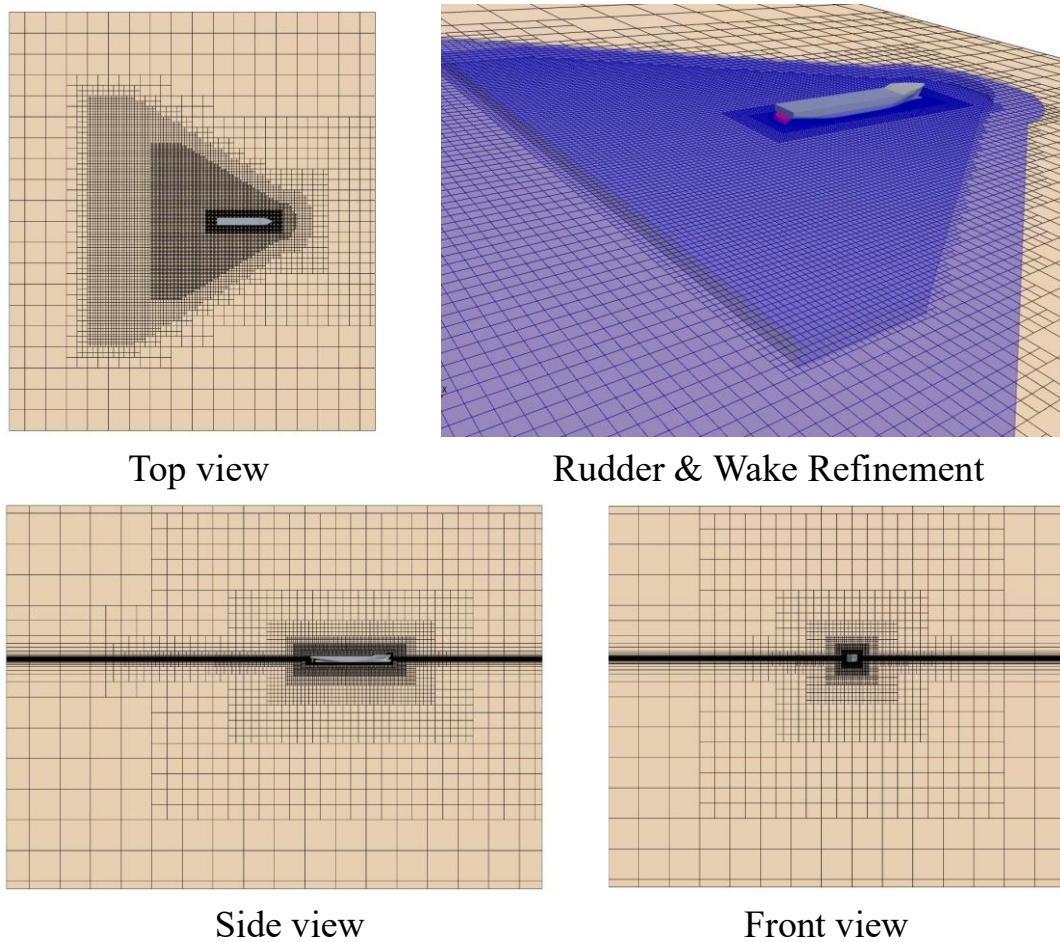


Fig. 3. Volume mesh generation and refinements

2.7 Controller

A controller was implemented to simulate the ship's manoeuvring. It was divided into two components: one for the propeller and another for the rudder, each controlled with different coefficients. Under self-propulsion conditions, the propeller controller was used to regulate the rps to achieve the target speed, while the rudder controller was employed to maintain the ship's heading angle at zero. The coefficients and structure of the controllers were designed based on (Song et al., 2024a; Choi et al., 2025; Min et al., 2025).

2.7.1 Propeller controller

The propeller controller employs a PI control method. The initial rotational speed was set to 11.5 rps, as used in the EFD. The target velocity was 2.006 m/s, matching the speed of the experimental ship. The rps of the self-propulsion point conducted in the experiment was 11.5, and the CFD-calculated rps was similarly 11.48, as shown in Table 3 and Fig. 4. In this study, the model self-propulsion point was used, and it was observed that the propeller rps under self-propulsion conditions varied depending on the trim conditions. The propeller controller was applied until the self-propulsion state was reached, after which only the final converged fixed rps was used in the manoeuvring simulation.

$$K_{P_{prop}} = 1/V_{design}, K_{I_{prop}} = 1.2/L_{pp}, n_0 = 11.5 \quad (3)$$

$$n = n_0 \left(1 + K_{P_{prop}} e_{speed} + K_{I_{prop}} \int_0^t e_{speed} dt \right) \quad (4)$$

$$e_{speed} = V_{target} - V_{ship} \quad (5)$$

Table 3 Propeller rps at the model self-propulsion point under different trim conditions

	Trim-by-Stern			Evenkeel	Trim-by-bow		
Trim angle(deg)	-3.00	-0.50	-0.25	0.00	0.25	0.50	2.00
n (rps)	13.11	11.38	11.51	11.48	11.46	11.53	11.49

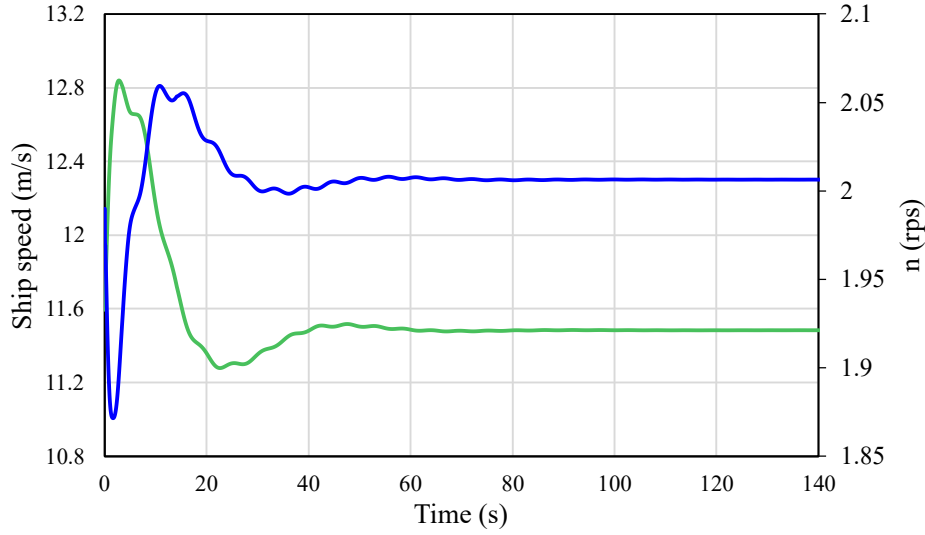


Fig. 4. Propeller rps and Ship Speed in Self-Propulsion Simulations

2.7.2 Rudder controller

The rudder controller is also used in self-propulsion and manoeuvring simulations to control ship motions. In the self-propulsion case, the target rudder angle is set to maintain the ship's heading angle at zero. This is because setting the actual rudder angle to zero would result in a non-zero heading due to the propeller rotation, as shown in Fig. 5. In turning or zigzag manoeuvres, the target angle is set to 30° or $\pm 20^\circ$. In cases of extreme rudder movement, the rudder rate may exceed the maximum allowable rate, potentially surpassing the $14.28^\circ/s$ limit suggested in SIMMAN 2020. To prevent this, a function that limits the rudder rate is implemented to ensure it remains within the allowable range.

$$K_{P_{rudder}} = 4, K_{I_{rudder}} = 0.6 V_{design}/L_{pp}, K_{D_{rudder}} = 1.3 L_{pp}/V_{design} \quad (6)$$

$$\delta_N = -K_{P_{rudder}} \psi - K_{I_{rudder}} \int_0^t \psi dt - K_{D_{rudder}} \dot{\psi} \quad (7)$$

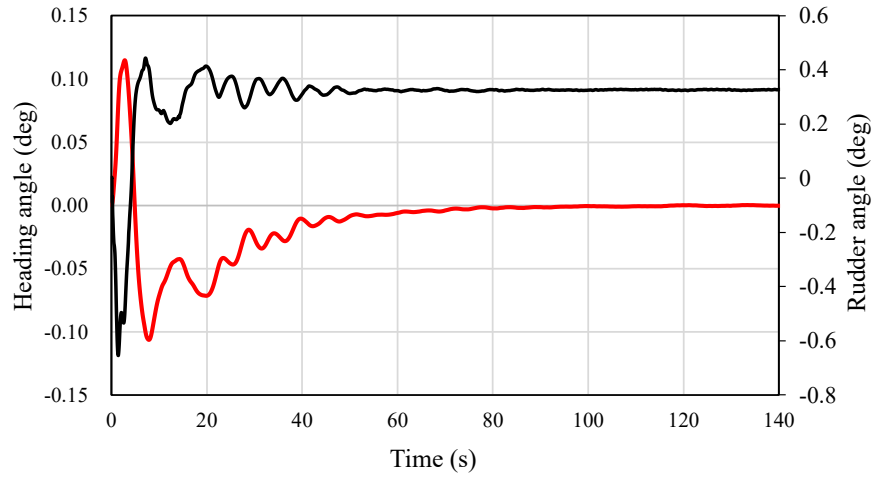


Fig. 5. Heading angle and rudder angle in self-propulsion simulations

3 Verification and Validation

3.1 Verification studies

To ensure the reliability of the simulations, spatial and temporal convergence studies were conducted using the Grid Convergence Index (GCI) proposed by Celik et al. (2008), as similarly utilised by recent studies (Kwon et al., 2023; Jung et al., 2022; Sun et al., 2024; Mikkelsen et al., 2022; Terziev et al., 2019; Grlj et al, 2024; Mikulec & Piehl, 2023). The spatial GCI was evaluated based on the fine mesh, while the temporal GCI was assessed using the mid time step in consideration of computational cost. Under the 35° portside turning condition, the Advance, Transfer, and Tactical Diameter all exhibited convergence within 1%, indicating sufficient numerical accuracy. The results of the GCI analysis are summarized in Table 4.

Table 4 Temporal and spatial grid convergence test results and total uncertainty

Spatial convergence	No. cells	Advance/Lpp	Transfer/Lpp	Tactical diameter/Lpp
Fine	3,447,875	2.8943	1.0742	2.5834
Mid	2,250,154	2.9018	1.0757	2.5792
Coarse	1,144,146	2.9249	1.1489	2.7665
	$U_{spatial} (GCI_{fine}, \%)$	0.4899	0.0173	0.0190
Temporal convergence	Time step	Advance/Lpp	Transfer/Lpp	Tactical diameter/Lpp
Fine	0.01	2.8972	1.0727	2.5736
Mid	0.02	2.8943	1.0742	2.5834
Coarse	0.04	2.9073	1.0585	2.5587
	$U_{temporal} (GCI_{mid}, \%)$	0.1612	0.2075	0.7890

Total uncertainty	Advance/Lpp	Transfer/Lpp	Tactical diameter/Lpp
U_{total} (%)	0.5157	0.2082	0.7892

3.2 Validation Studies

To validate the reliability of the simulation results, comparisons were made with experimental data obtained from MARIN. Validation was performed for the trajectory, roll angle, surge speed, and yaw rate during both the 35° portside turning test and the 20°/20° portside zigzag manoeuvre. In the 35° portside turning test, the simulation showed high accuracy, with a maximum error of 2.1% in Advance, Transfer, and Tactical Diameter, as summarized in Table 5. The turning trajectory comparison is illustrated in Fig. 6. The roll angle was slightly underestimated, while the surge speed was marginally overestimated, as shown in Fig. 7.

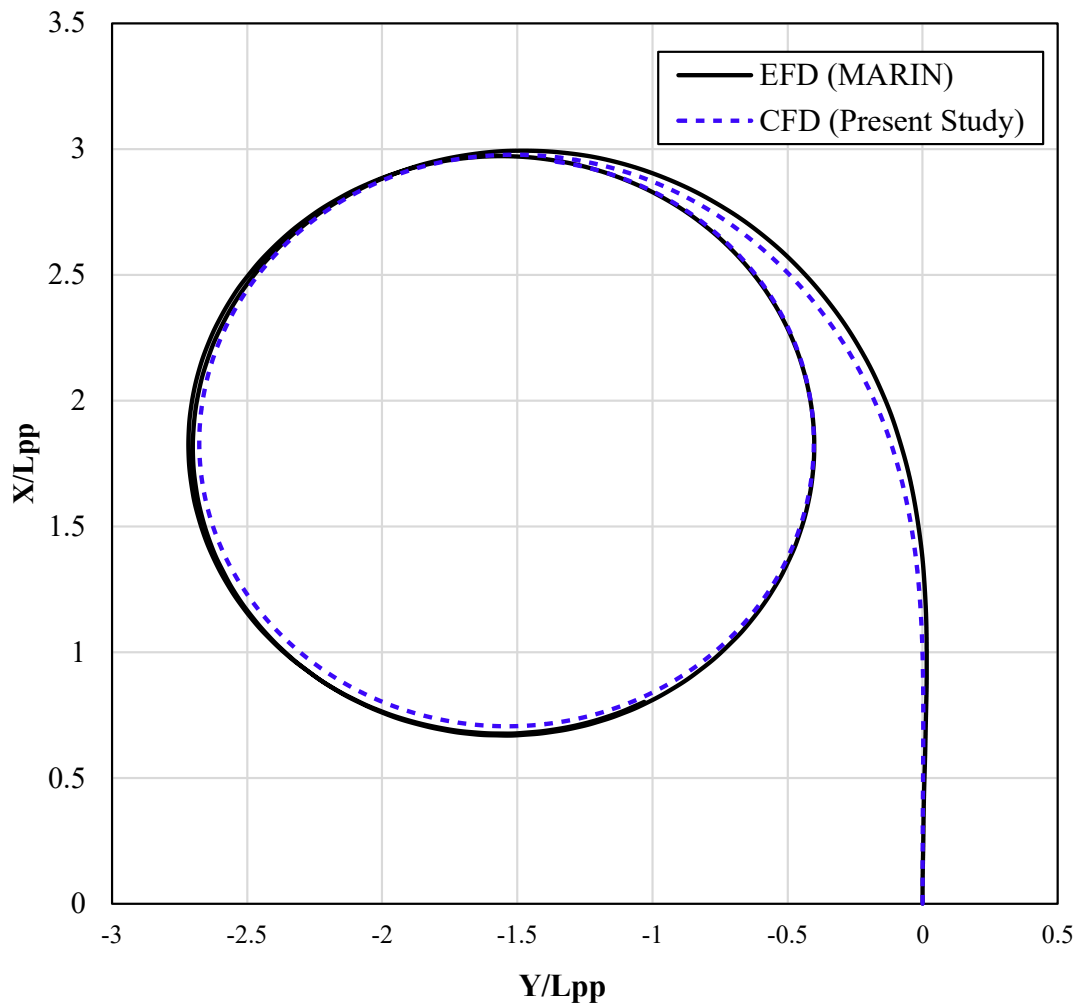
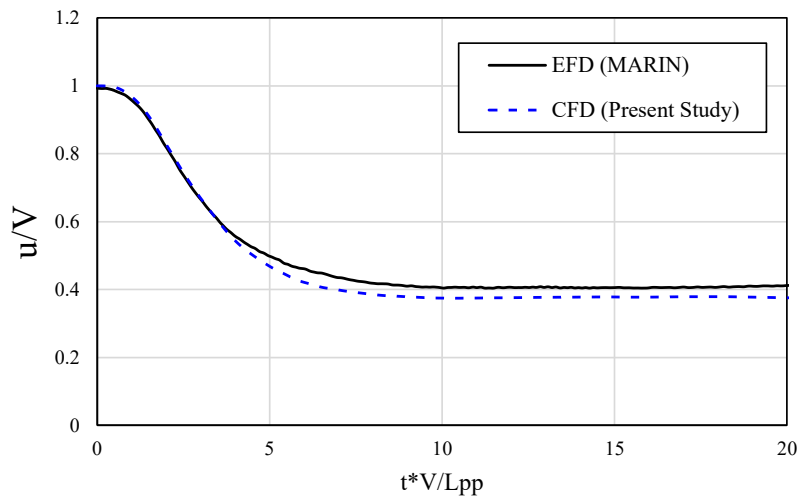
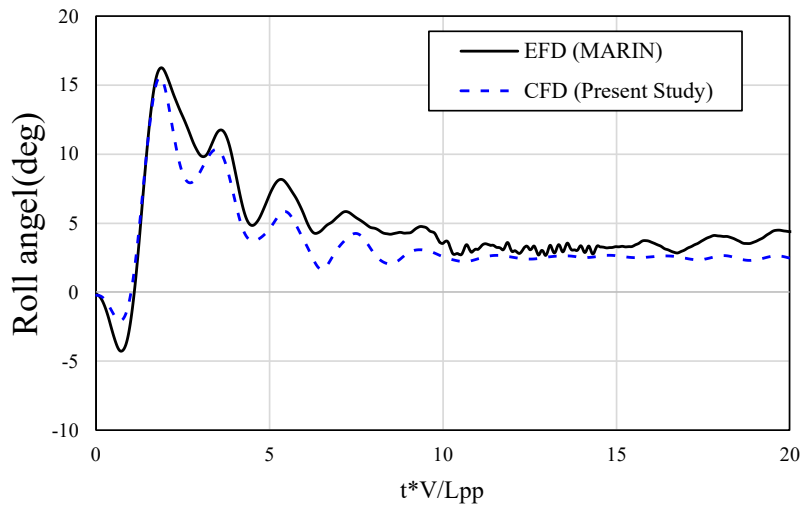


Fig. 6. 35° Portside Turning circle trajectory in even-keel condition (EFD & CFD)

Table 5 Key indices of 35° portside turning circle in even-keel Condition (EFD & CFD)

	Transfer/Lpp	Advance/Lpp	Tactical diameter/Lpp
CFD (MARIN)	1.0854	2.9341	2.6401
EFD (Present Study)	1.0742	2.8943	2.5834
Difference(%)	1.0335	1.3562	2.1485



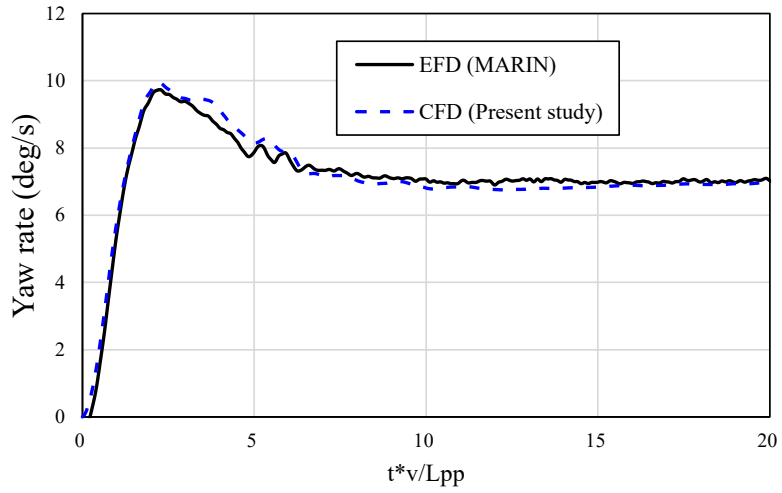


Fig. 7. Roll angle, surge speed and yaw rate - 35° portside turning circle in even-keel condition (EFD & CFD)

During the 20°/20° zigzag manoeuvre, the second and third overshoot angles were overestimated by approximately 11% compared to the first overshoot angle, as shown in Table 6. In contrast, the roll angle and surge speed showed better agreement with the experimental data than in the turning test. The zigzag trajectory is illustrated in Fig. 8, while the roll angle, surge speed, and yaw rate are presented in Fig. 9.

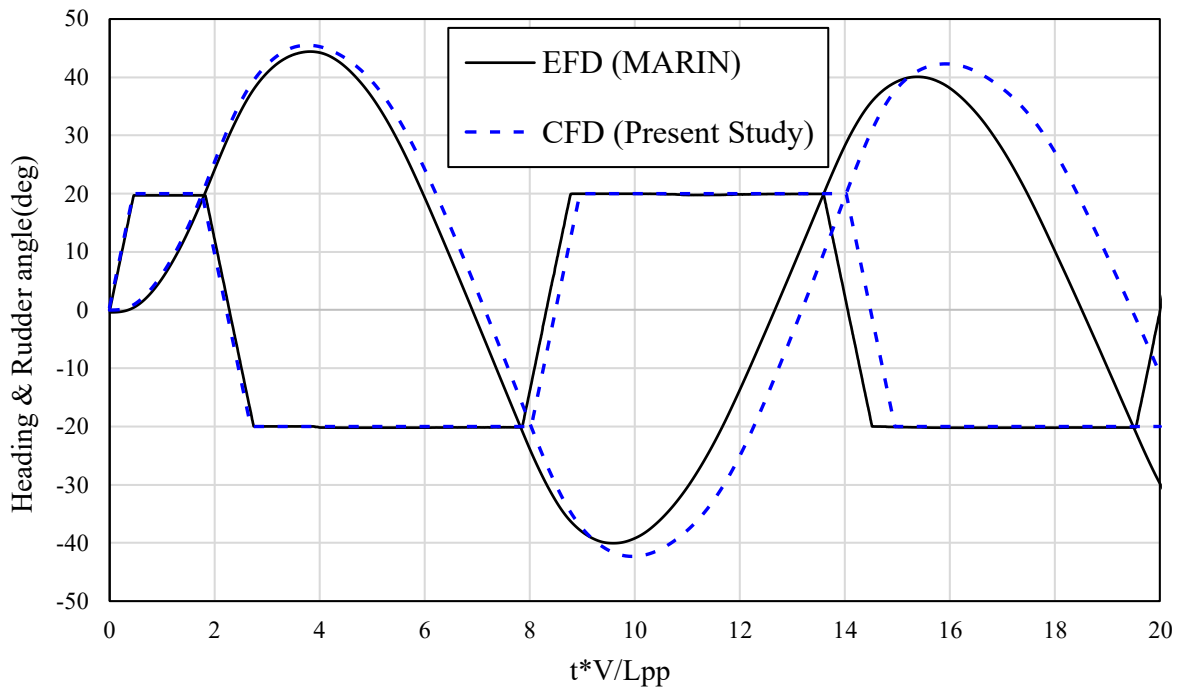
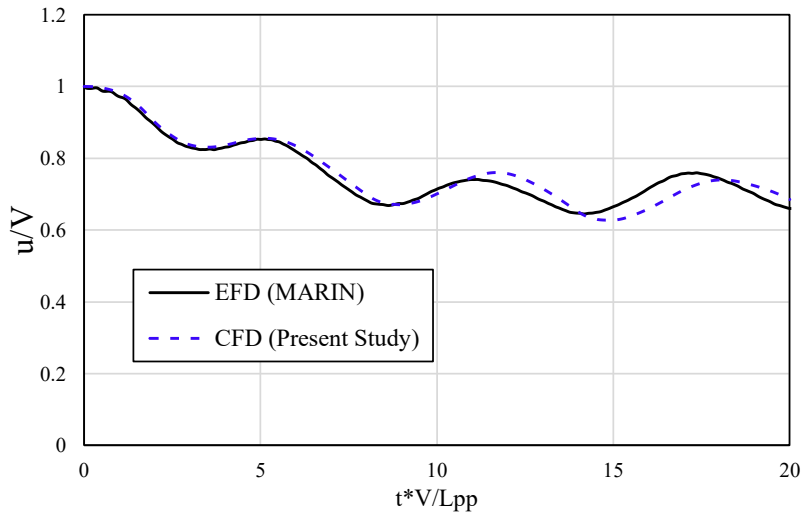
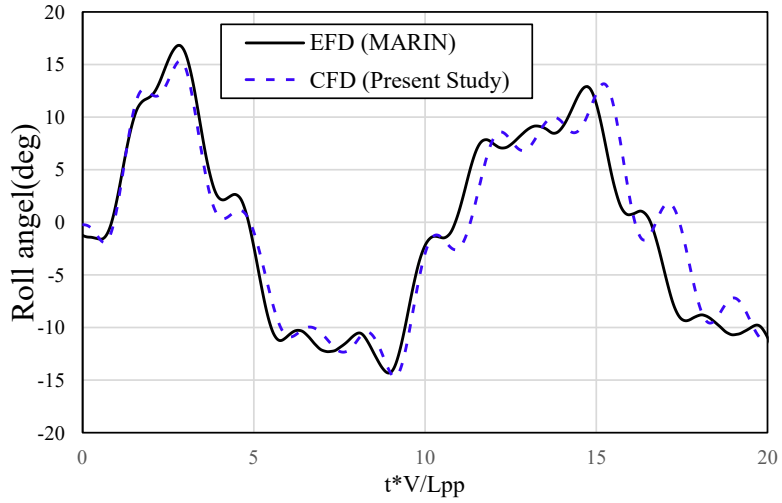


Fig. 8. 20°/20° portside zigzag trajectory in even-keel condition (EFD & CFD)

Table 6 Key indices of 20°/20° portside zigzag in even-keel condition (EFD & CFD)

	1 st overshoot angle(deg)	2 nd overshoot angle(deg)	3 rd overshoot angle(deg)
CFD (MARIN)	25.491	22.309	22.289
EFD (Present Study)	24.398	20.044	20.061
Difference(%)	4.482	11.301	11.103



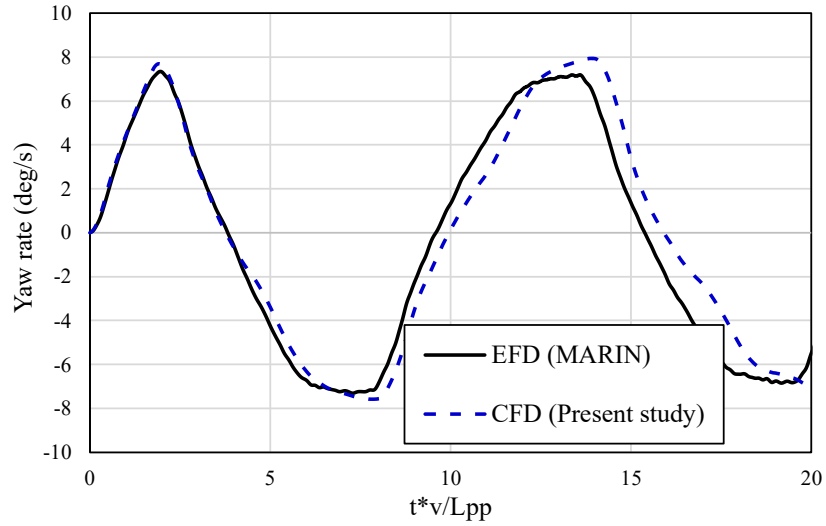
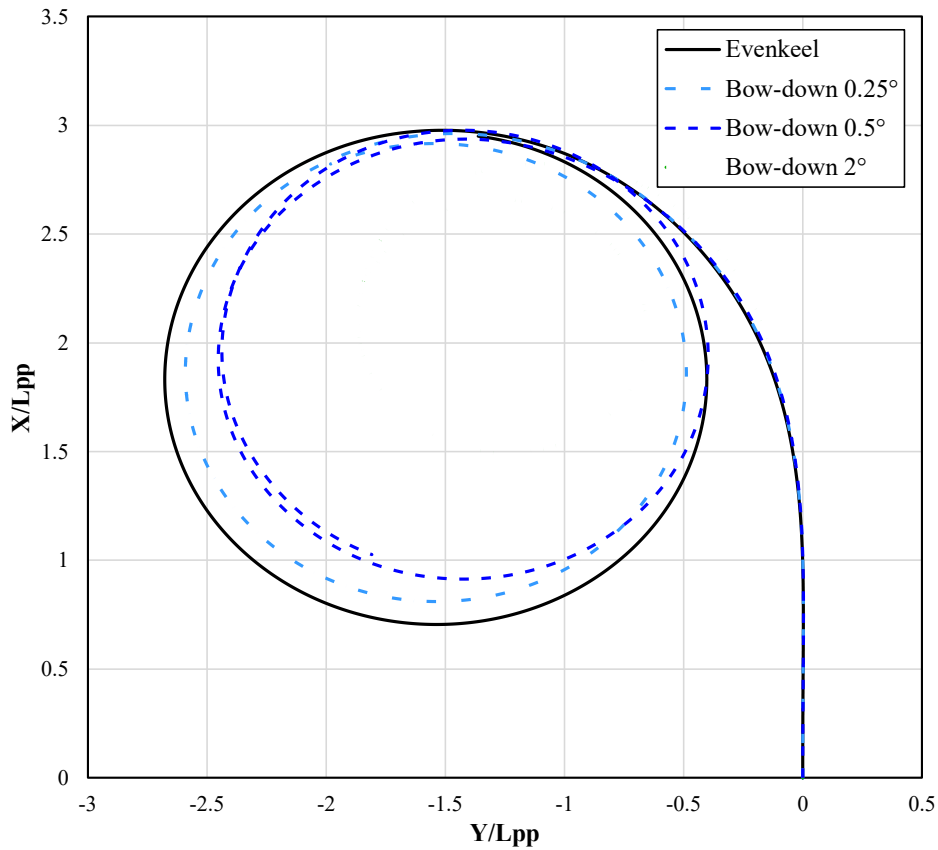


Fig. 9. Roll angle, surge speed and yaw rate - 35° 20°/20° portside zigzag in even-keel condition (EFD & CFD)

4 Results

The results section presents how the 35° port turning circle and zigzag manoeuvring vary depending on the trim conditions. As the trim by bow increases, the turning circle trajectory becomes smaller, and the overshoot angle is reduced. Conversely, as the trim by stern becomes more pronounced, the opposite trend is observed. The analysis and interpretation of these results are provided in the following subsections.

4.1 35° Portside turning circle manoeuvre



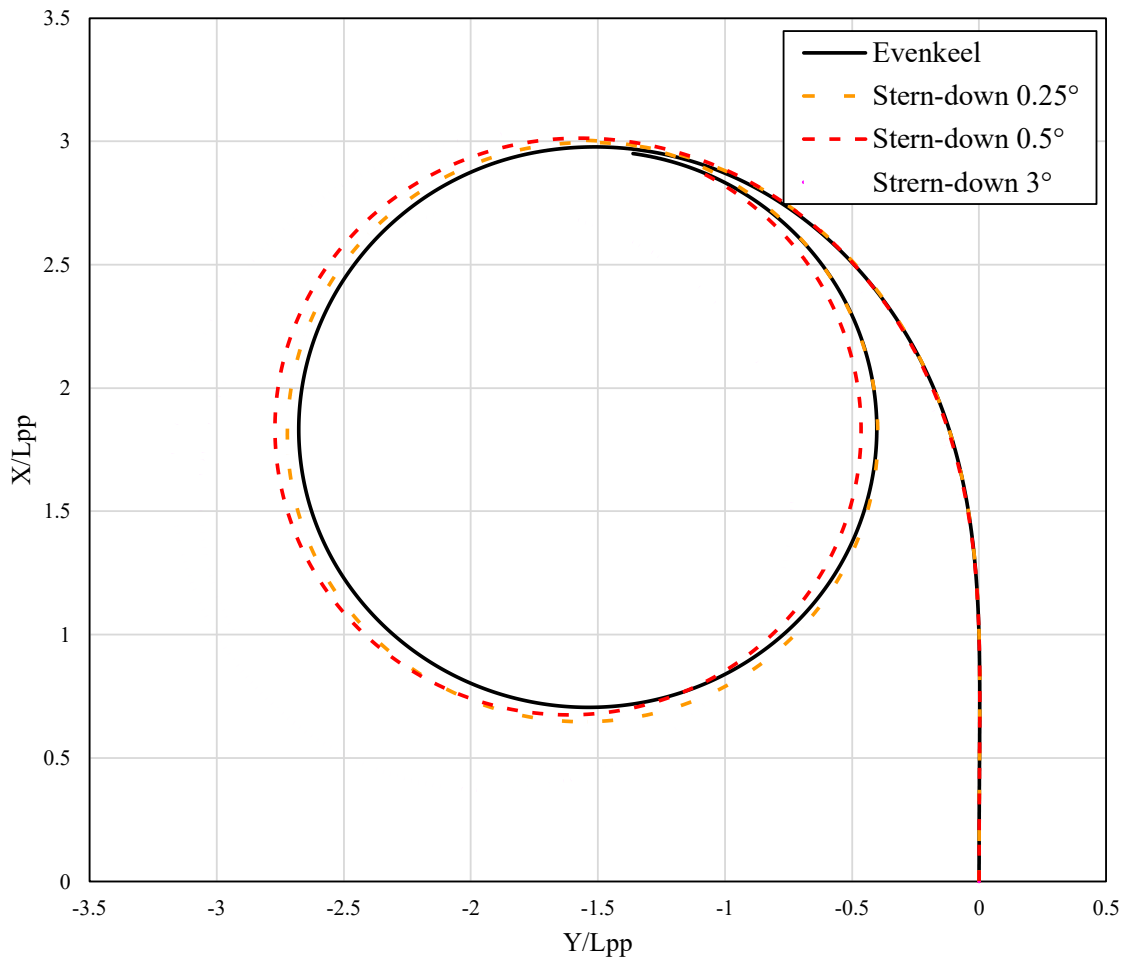


Fig. 10. 35° Portside turning circle trajectory under various trim conditions

Table 7 Key indices of 35° portside turning circle under various trim conditions

	Transfer/Lpp	Advance/Lpp	Tactical diameter/Lpp
Bow-down 2°	0.695	2.737	1.746
Bow-down 0.5°	0.999	2.854	2.365
Bow-down 0.25°	1.034	2.882	2.510
Evenkeel	1.074	2.894	2.583
Stern-down 0.25°	1.099	2.920	2.635
Stern-down 0.5°	1.137	2.939	2.688
Stern-down 3°	1.299	2.967	3.097

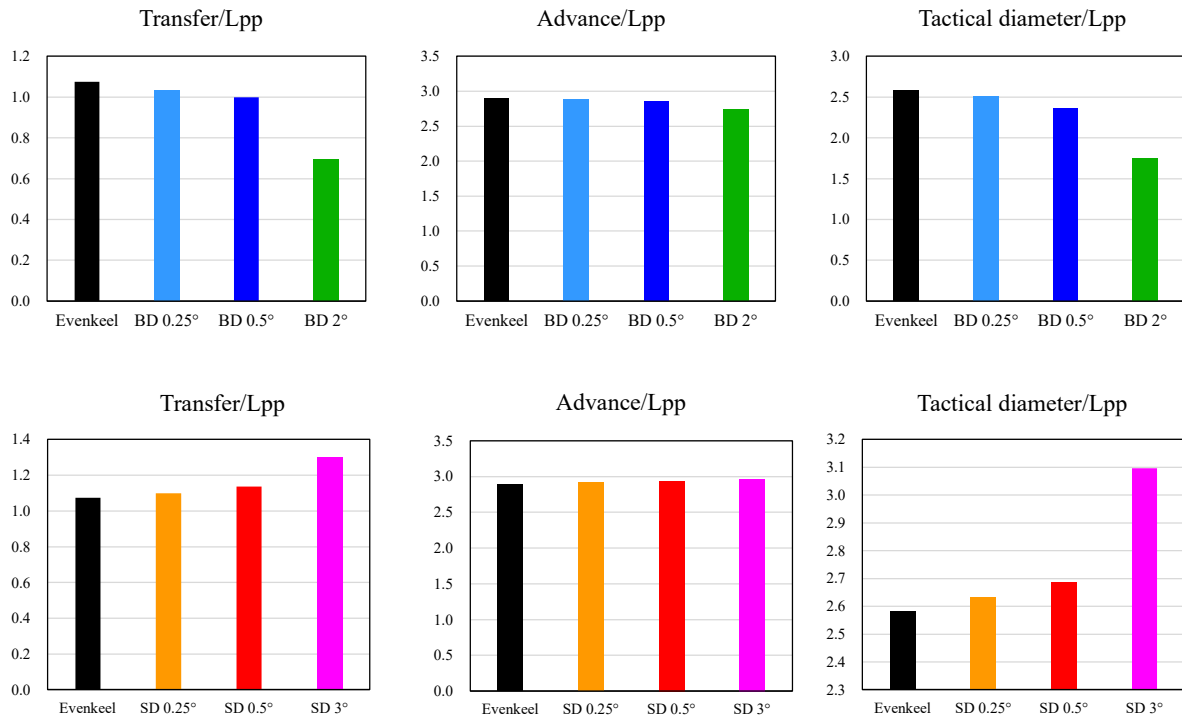
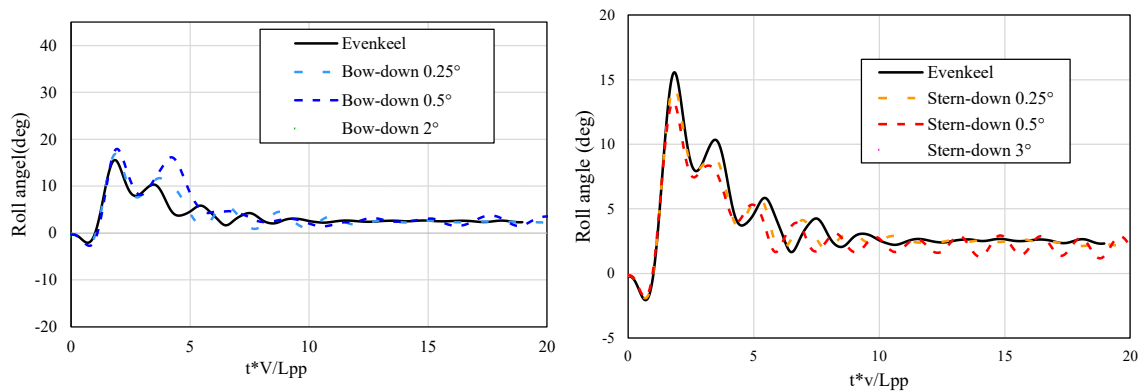


Fig. 11. Comparison of key indices for each case during 35° portside turning

Fig. 10. presents the turning circle trajectories for both the three bow-down and three stern-down trim cases. It is evident that as the bow-down trim increases, the turning radius decreases significantly. Correspondingly, the transfer, advance, and tactical diameters all decrease, as shown in Table 7 and Fig. 11. Among these, the tactical diameter exhibits the most pronounced reduction at larger bow-down trim angles. This indicates that under bow-down trim conditions, the ship tends to turn more inward compared to the even-keel state. Conversely, in the stern-down trim cases, which demonstrate the opposite trend, the turning circle diameter increases with greater stern-down trim. The transfer, advance, and tactical diameters all increase accordingly, with the tactical diameter showing the largest growth at higher stern-down trims.



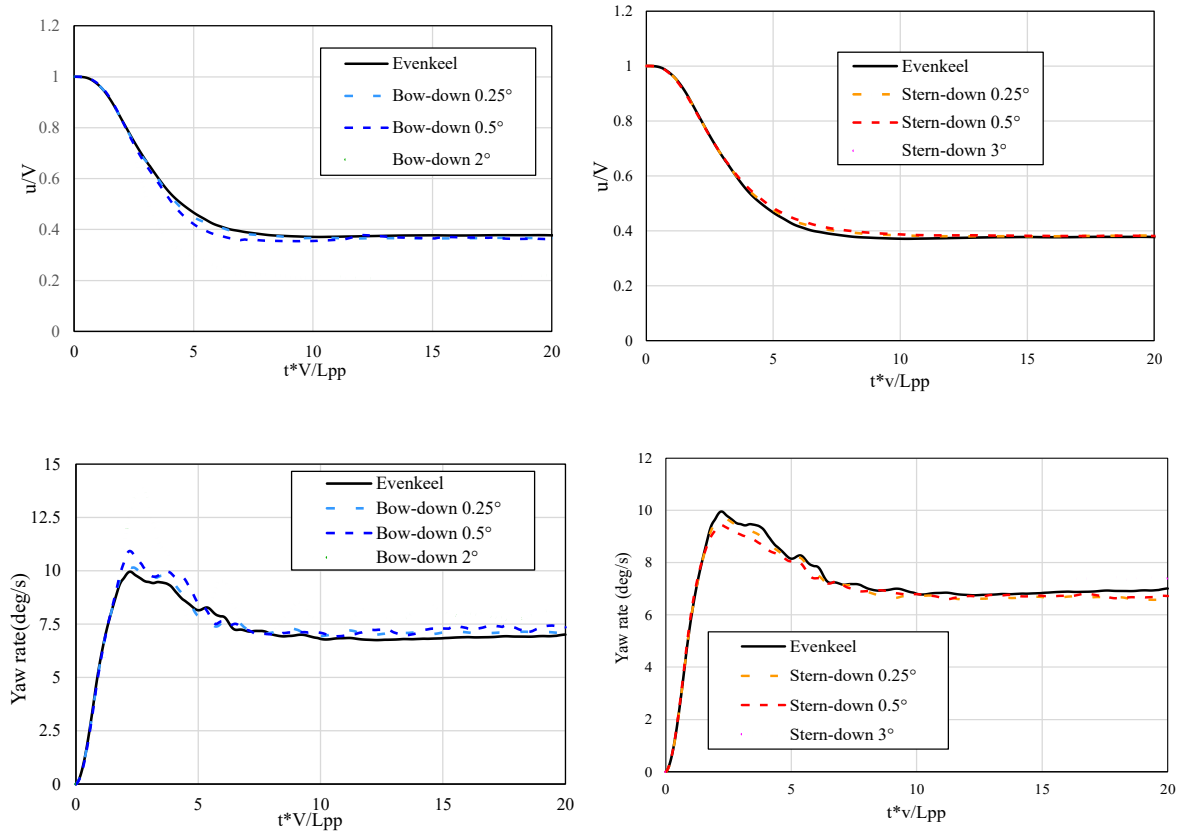


Fig. 12. Comparison of roll angle, surge speed and yaw rate under various trim conditions during a 35° portside turning manoeuvre

Fig. 12 shows the roll angle, surge speed, and yaw rate under various conditions. As the bow-down trim increases, the roll angle increases significantly, suggesting a notable reduction in the ship's stability during turning manoeuvres under bow-down conditions. Meanwhile, the surge speed decreases, likely because the ship pushes water forward at the bow, generating a large hydrodynamic force that reduces its speed. Additionally, the decrease in surge speed is believed to have partially contributed to the reduction in turning radius. The yaw rate also increases as the bow-down trim becomes more severe. Furthermore, the initial yaw rate increases more than the converged yaw rate.

The observed trends of increasing roll angle, decreasing surge speed, and increasing yaw rate under bow-down conditions are consistent with previous studies (e.g., Himaya et al., 2022; Yun et al., 2020). These changes in roll angle are primarily influenced by variations in the ship's waterplane area caused by trim conditions, which subsequently affect the metacentric height (GM) and the vessel's stability characteristics. This can be confirmed in Table 2, where the Bow-down 2° case shows a very small GM value, which is predicted to cause abnormal roll angles.

In contrast, under stern-down trim conditions, the roll angle and surge speed exhibit opposite trends: as the stern-down trim increases, the roll angle decreases while the surge speed tends to increase. Furthermore, the initial yaw rate tends to decrease in this case, which can be attributed to the bow rising and thus reducing the hydrodynamic Y-force acting on the bow compared to the even-keel condition, while the Y-force at the stern increases.

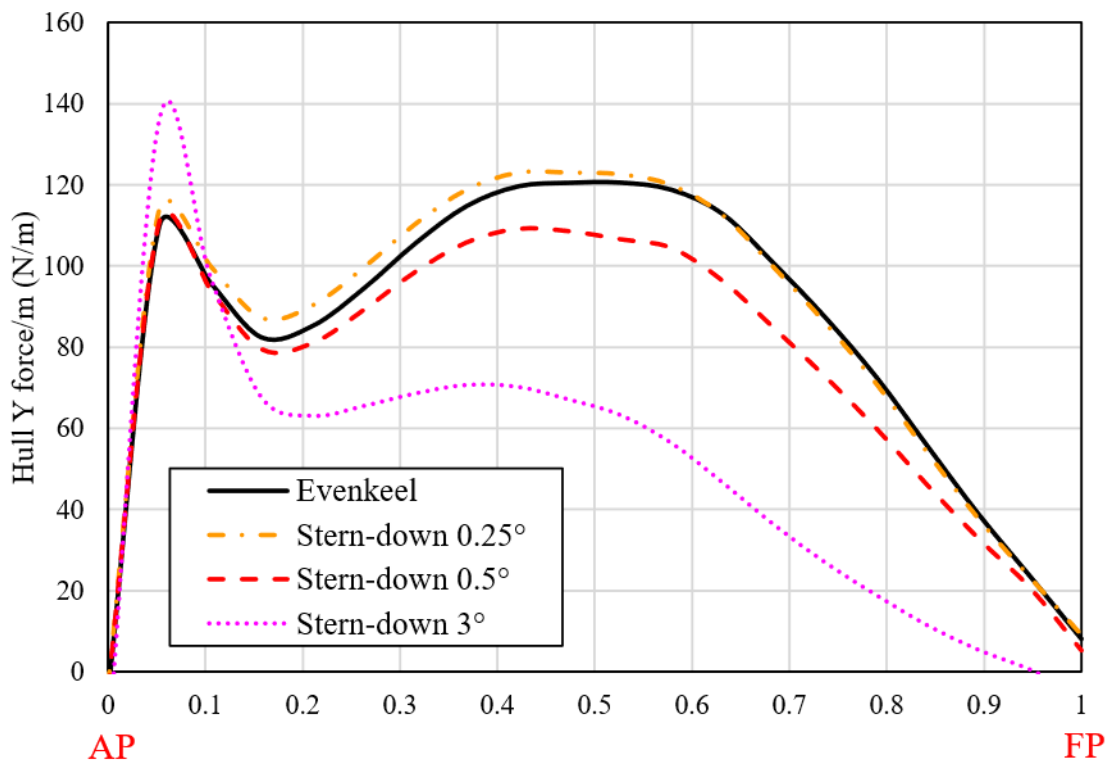
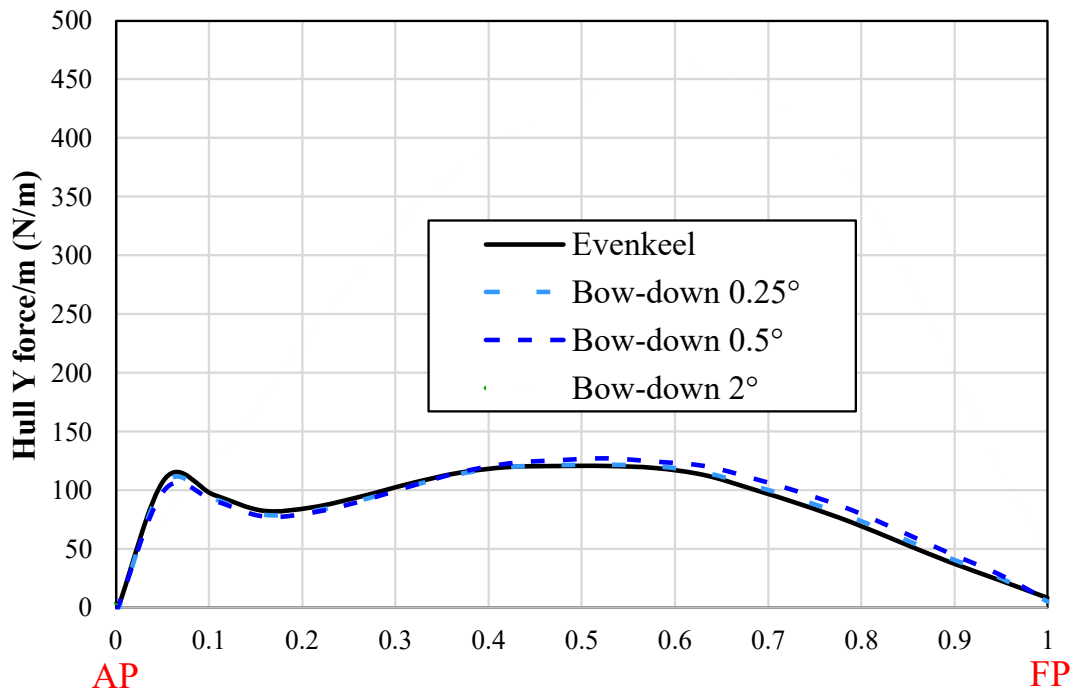


Fig. 13. Hull-Y force distribution along the ship length at steady state

Table 8 Position of Centre of the gravity & hull Y force

	Centre of gravity (m)	Centre of hull Y force (m)	Length* (m)
Bow-down 2°	3.169	3.261	0.093
Bow-down 0.5°	2.956	2.881	-0.075
Bow-down 0.25°	2.938	2.830	-0.108
Evenkeel	2.914	2.787	-0.127
Stern-down 0.25°	2.889	2.753	-0.137
Stern-down 0.5°	2.871	2.702	-0.169
Stern-down 3°	2.744	2.152	-0.592

*Lenth indicates the distance between centre of gravity and centre of hull Y force which represent the yawing moments

Fig. 13. shows the distribution of the Y-force acting on the ship along its length from the aft perpendicular (AP) to the forward perpendicular (FP) when the forces reach a steady state during a turning manoeuvre. The Y-force is measured in the ship-fixed coordinate system, with the portside direction defined as positive. As the bow-down trim increases, it can be observed that the magnitude of the force acting near the bow increases. This means that both the ship's centre of gravity and the centre of hydrodynamic forces move toward the bow. Consequently, the effective moment arm for the yaw moment increases, which explains the expected increase in yaw rate. Furthermore, in the case of the 2° bow-down trim, the magnitude of the force is particularly large. A stronger Y-direction force allows the ship to maintain a consistently smaller turning radius.

Conversely, in the stern-down cases both the ship's centre of gravity and the centre of the Y-direction hydrodynamic force shift toward the stern. As a result, the effective moment arm for the yaw moment decreases, which is expected to cause the initial yaw rate to decrease. This reduction in initial yaw rate is expected to result in a significant increase in the tactical diameter.

Table 8 presents the positions of the centre of gravity (COG) and the centre of hull Y-force measured from the aft perpendicular (AP). In the case of bow-down trim, the centre of hull Y-force is located either toward the bow relative to the COG or slightly toward the stern. However, for stern-down trim, the centre of hull Y-force is noticeably shifted toward the stern compared to the COG. This result is considered an important indicator for understanding the trends observed in the ship's trajectory.

4.2 20°/20° portside zigzag manoeuvre

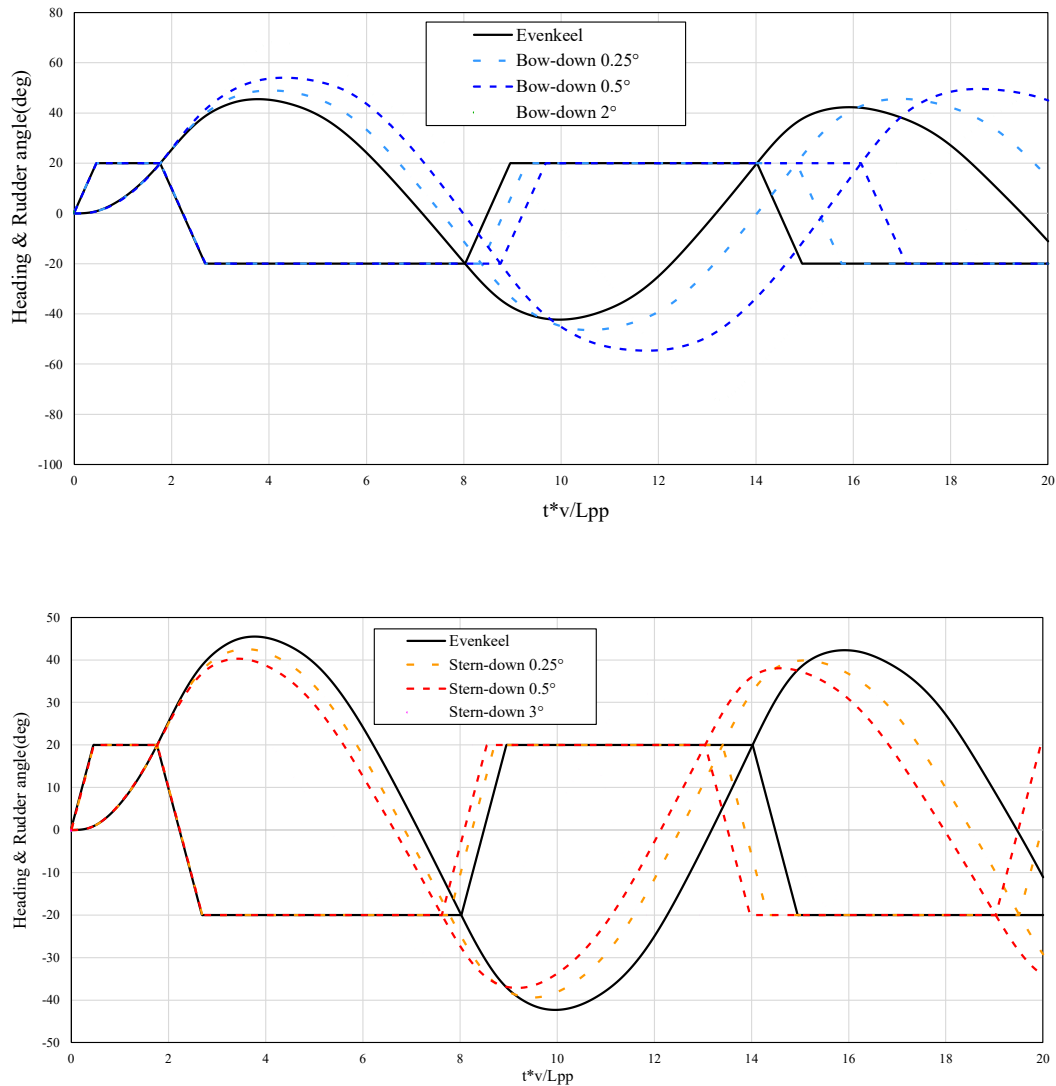


Fig. 14. 20°/20° portside zigzag trajectory under various trim conditions

Table 9 Key indices of 20°/20° portside zigzag under various trim conditions

	1 st overshoot angle(deg)	2 nd overshoot angle(deg)	3 rd overshoot angle(deg)
Bow-down 2°	47.939	54.092	40.571
Bow-down 0.5°	34.034	34.652	29.560
Bow-down 0.25°	28.949	26.453	25.608
Evenkeel	25.491	22.309	22.289
Stern-down 0.25°	22.544	19.402	19.881
Stern-down 0.5°	20.288	17.145	18.048
Stern-down 3°	12.309	9.802	12.216

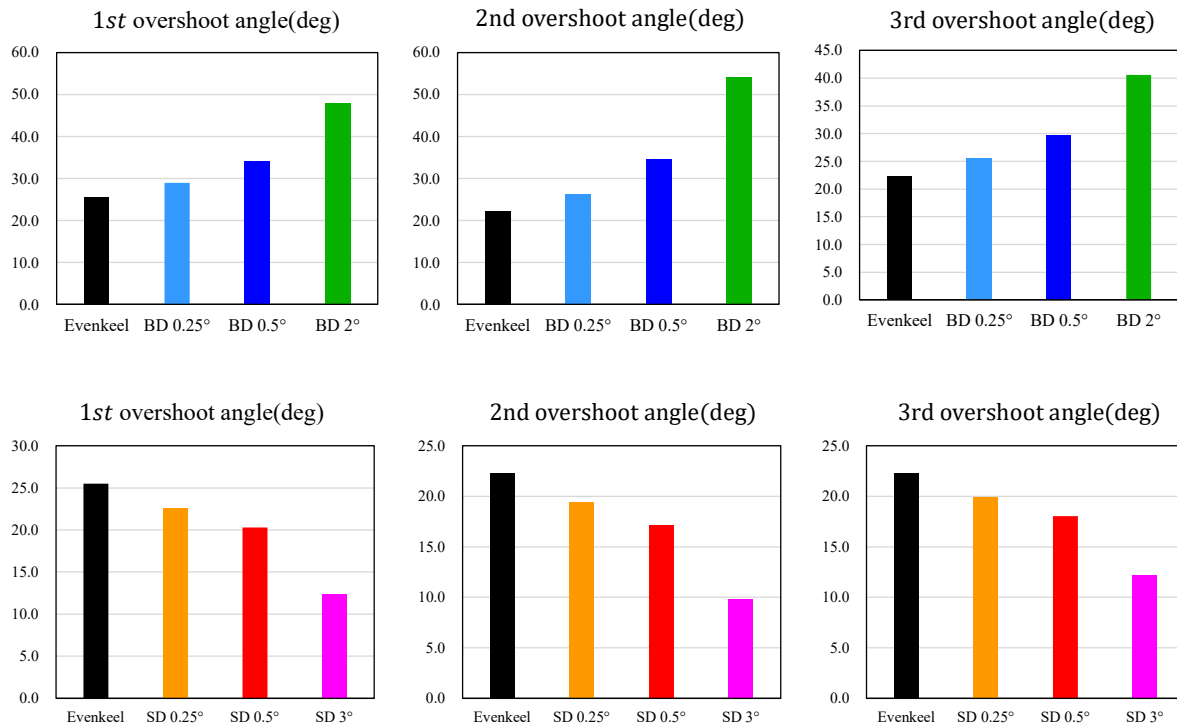


Fig. 15. Comparison of key indices for each case during 20°/20° portside zigzag

During the zigzag test, it was observed that the overshoot angle increases as the bow-down trim becomes more severe. In particular, under the 2° bow-down trim condition, the ship's behaviour appears highly unstable. This instability is attributed to the significantly increased roll angle during the zigzag manoeuvre, which makes normal steering difficult. Conversely, in the stern-down condition, the overshoot angle decreases as the stern-down trim becomes more severe. These trends are clearly illustrated in the trajectory plots shown in Fig. 14, and the associated key manoeuvring indices are summarized in Table 9. A comparison of these indices for each trim condition is further highlighted in Fig. 15.

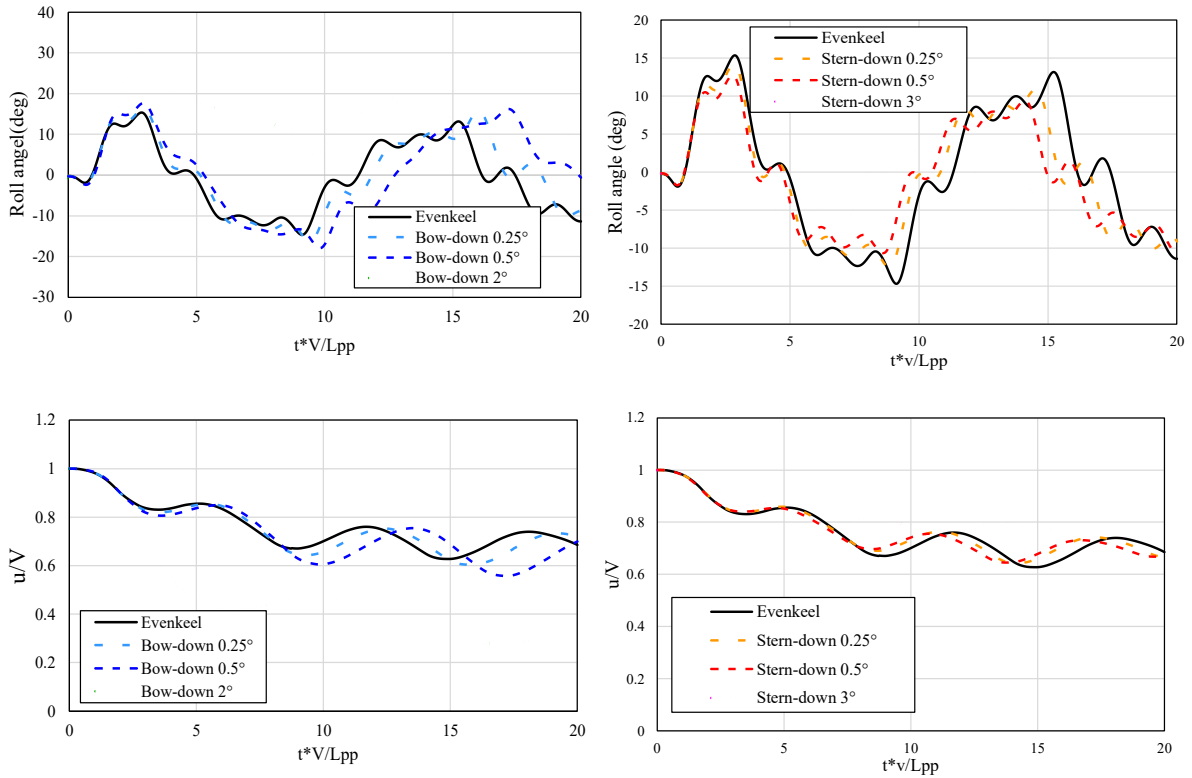
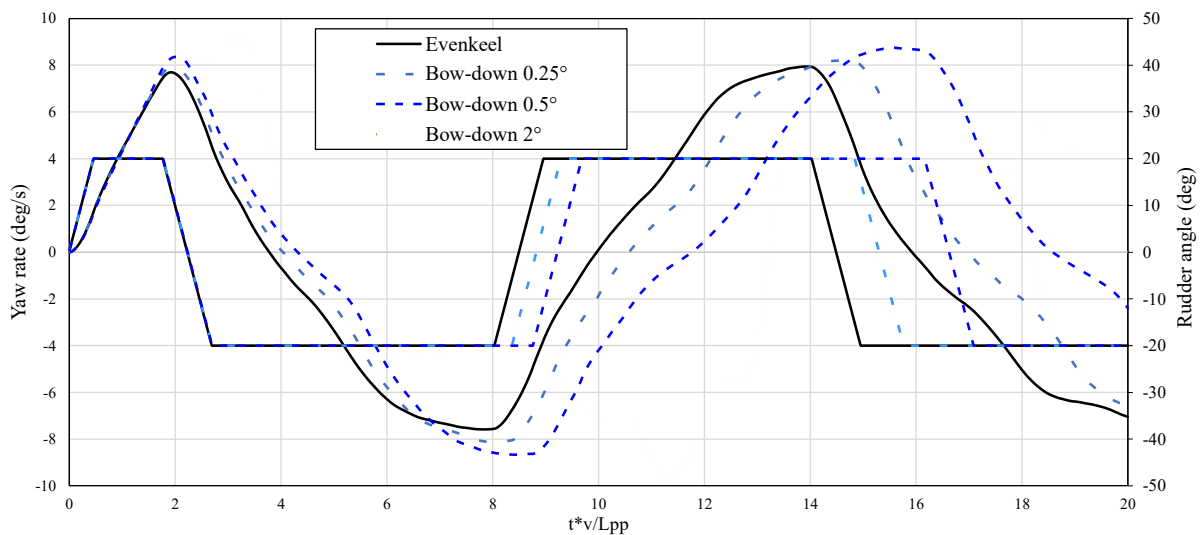


Fig. 16. Comparison of roll angle and surge speed during 20°/20° portside zigzag manoeuvre

The roll angle and surge speed showed similar trends to those observed in the turning test results. As the bow-down trim increased, the roll angle increased while the surge speed tended to decrease. Conversely, in the stern-down condition, the roll angle decreased, and the surge speed increased. This trend is consistent with the results observed in the turning circle test and is clearly illustrated in Fig. 16.



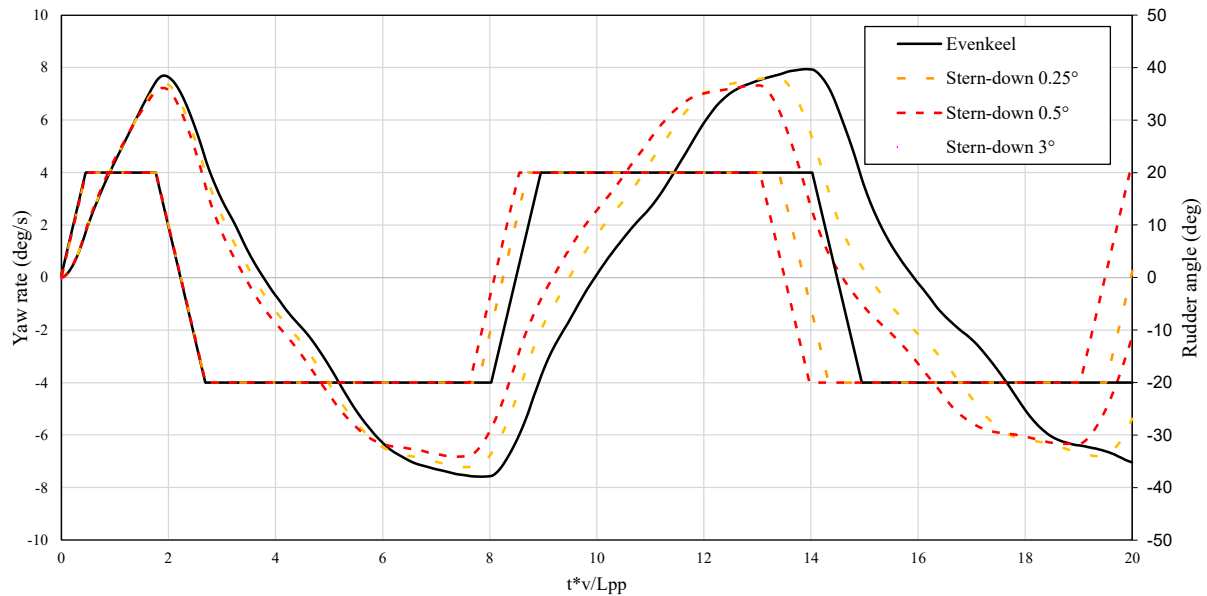


Fig. 17. Yaw rate and rudder angle during the 20°/20° portside zigzag manoeuvre under various trim conditions

The yaw rate and rudder angle during the zigzag test are shown in Fig. 17. The points at which the heading angle initially reaches 20° are nearly identical across all cases, which explains why the rudder reverses direction at similar times. As the bow-down trim increases, the yaw rate decays more slowly following rudder reversal, and the peak yaw rate becomes higher than that observed under even-keel conditions. These combined effects are considered to contribute to the increased overshoot angles. In particular, under the 2° bow-down trim condition, the yaw rate distribution appears abnormal, likely due to the excessive trim making normal steering difficult.

During the zigzag test under stern-down conditions, the yaw rate and rudder angle behaved as follows. Although the points where the rudder reverses direction are similar, as the stern-down trim becomes more severe, the yaw rate decreases sharply after the rudder reversal. This corresponds to the observed tendency for the overshoot angle to decrease.

5 Conclusion

In the case of bow-down trim, the turning tests showed that advance, transfer, and tactical diameter decreased, with the tactical diameter showing the largest reduction at large trim angles. This reduction in turning circle is attributed to the increase in hull Y-force and yaw rate. This phenomenon is characterized by a forward shift of both the ship's centre of gravity and the hydrodynamic Y-force distribution toward the bow, which leads to enhanced rotational motion. The change in Y-force distribution is more pronounced in bow-down trim compared to stern-down conditions.

In the zigzag tests, bow-down trim resulted in an increase in the peak yaw rate, and the yaw rate did not decrease immediately when the rudder reversed direction. This delayed response contributed to larger overshoot angles and increased instability in manoeuvring, particularly in the 2° bow-down case where the ship roll motion appeared abnormal. The roll angle increased due to reduced metacentric height (GM) values caused by changes in waterplane area.

Conversely, stern-down trim showed opposing trends across all measured parameters and manoeuvring characteristics. During turning tests, advance, transfer, and tactical diameter all showed increasing tendencies with stern-down trim, with the tactical diameter showing the largest increase at large trim angles. The large turning circle diameter is governed by decreased initial yaw rate and Y-force at the bow due to the shift of both the centre of gravity and hydrodynamic force distribution toward the stern. The reduction in hydrodynamic Y-force at the bow, combined with the increase at the stern, creates a smaller effective moment arm for yaw motion, leading to decreased rotational capability and larger turning circles.

In the zigzag tests, stern-down trim resulted in a decrease in the peak yaw rate during the manoeuvre, and the yaw rate rapidly decreased immediately following rudder reversal. This prompt response contributed to smaller overshoot angles and more stable manoeuvring compared to bow-down conditions. The roll angle was observed to decrease, which is attributed to increased metacentric height (GM) values caused by changes in waterplane area.

Analysis of these results shows that under small trim angles commonly encountered in practice, trim-by-stern provides better manoeuvrability in turning manoeuvres, while trim-by-bow demonstrates superior performance in zigzag tests. However, it is essential to note that trim conditions can cause ship motions (e.g., roll angle, surge speed, yaw rate) to become either excessive or insufficient compared to expected motion responses, which must be carefully considered.

In this study, the body-propeller method was employed for manoeuvring analysis. Under stern-down trim conditions, however, the propeller is positioned closer to the free surface than in the even-keel condition, potentially leading to discrepancies between actual propeller performance and the assumed model behaviour, which represents a limitation of the present study. Additionally, the present analysis focused solely on the manoeuvring performance under varying trim conditions. While the current analysis focused solely on trim variations, future studies will extend this work by examining the effects of other attitude changes such as draft variation, heel angle, and combined motions on manoeuvring performance.

6 Acknowledgements

This work was supported by the Technology Innovation Program (RS-2024-00508368) funded by the Ministry of Trade, Industry & Energy (MOTIE, Korea)

7 References

- Park, D. W., Lee, S. B., Chung, S. S., Seo, H. W., & Kwon, J.-W. (2013, April 20). Effects of Trim on Resistance Performance of a Ship. *Journal of the Society of Naval Architects of Korea*. The Society of Naval Architects of Korea. <https://doi.org/10.3744/snak.2013.50.2.88>
- Dae-Won Seo, Hyun-Suk Park, & Ki-Min Han. (2015). Analysis of resistance performance for various trim conditions on container ship using CFD. *Journal of Ocean Engineering and Technology*, 29(3), 224-230.
- Han, Ki-Min, Park, Hyun-Suk, & Seo, Dae-Won. (2015). Study on Resistance Component of Container Ship According to Trim Conditions. *Journal of Ocean Engineering and Technology*, 29(6), 411-417. <https://doi.org/10.5574/KSOE.2015.29.6.411>
- Le, T. H., Vu, M. T., Bich, V. N., Phuong, N. K., Ha, N. T. H., Chuan, T. Q., & Tu, T. N. (2021). Numerical investigation on the effect of trim on ship resistance by RANSE method. *Applied Ocean Research*, 111, 102642.
- Sherbaz, S., & Duan, W. (2014). Ship trim optimization: assessment of influence of trim on resistance of MOERI container ship. *The Scientific World Journal*, 2014(1), 603695.
- Carrica, P. M., Mofidi, A., Eloot, K., & Delefortrie, G. (2016). Direct simulation and experimental study of zigzag maneuver of KCS in shallow water. *Ocean engineering*, 112, 117-133.
- Carrica, P. M., Castro, A. M., & Stern, F. (2010). Self-propulsion computations using a speed controller and a discretized propeller with dynamic overset grids. *Journal of marine science and technology*, 15, 316-330.
- Castro, A. M., Carrica, P. M., & Stern, F. (2011). Full scale self-propulsion computations using discretized propeller for the KRISO container ship KCS. *Computers & fluids*, 51(1), 35-47.
- Song, S., Choi, W. S., Eom, M. J., Kim, M. H., & Kim, B. G. (2024b). Townsin's formula vs CFD: Evaluating hull roughness effect in ship resistance. *Ocean Engineering*, 303, 117754.
- Lee, S. H., Paik, K. J., Hwang, H. S., Eom, M. J., & Kim, S. H. (2021). A study on ship performance in waves using a RANS solver, part 1: Comparison of power prediction methods in regular waves. *Ocean Engineering*, 227, 108900.
- He, T., Feng, D., Liu, L., Wang, X., & Jiang, H. (2022). CFD simulation and experimental study on coupled motion response of ship with tank in beam waves. *Journal of Marine Science and Engineering*, 10(1), 113.
- Huang, S., Jiao, J., & Soares, C. G. (2022). Uncertainty analyses on the CFD-FEA co-simulations of ship wave loads and whipping responses. *Marine Structures*, 82, 103129.
- Mikulec, M., & Piehl, H. (2023). Verification and validation of CFD simulations with full-scale ship speed/power trial data. *Brodogradnja: An International Journal of Naval Architecture and Ocean Engineering for Research and Development*, 74(1), 41-62.
- Shen, Z., Wan, D., & Carrica, P. M. (2015). Dynamic overset grids in OpenFOAM with application to KCS self-propulsion and maneuvering. *Ocean Engineering*, 108, 287-306.

- Song, S., Kim, D., & Dai, S. (2024a). CFD investigation into the effect of GM variations on ship manoeuvring characteristics. *Ocean Engineering*, 291, 116472.
- Yun, K., Kim, D. J., & Yeo, D. J. (2020, August 20). An Experimental Study on the Manoeuvrability of a Ship in Different GM and Trim Conditions. *Journal of the Society of Naval Architects of Korea*. The Society of Naval Architects of Korea. <https://doi.org/10.3744/snak.2020.57.4.230>
- Himaya, A. N., Sano, M., Suzuki, T., Shirai, M., Hirata, N., Matsuda, A., & Yasukawa, H. (2022). Effect of the loading conditions on the maneuverability of a container ship. *Ocean Engineering*, 247, 109964.
- Kim, D., Song, S., Jeong, B., & Tezdogan, T. (2021). Numerical evaluation of a ship's manoeuvrability and course keeping control under various wave conditions using CFD. *Ocean Engineering*, 237, 109615.
- Kim, H., Kim, S., Lee, K., Yoon, H., Lee, H., & Song, C. (2025). A Study on the Evaluation of Turning Performance of Small Fishing Vessels. *Journal of the Korean Society of Marine Environment & Safety*, 31(1), 96-108.
- Araki, M., Sadat-Hosseini, H., Sanada, Y., Tanimoto, K., Umeda, N., & Stern, F. (2012). Estimating maneuvering coefficients using system identification methods with experimental, system-based, and CFD free-running trial data. *Ocean Engineering*, 51, 63-84.
- Li, S., Liu, C., Chu, X., Zheng, M., Wang, Z., & Kan, J. (2022). Ship maneuverability modeling and numerical prediction using CFD with body force propeller. *Ocean Engineering*, 264, 112454.
- Jiang, L., Yao, J., & Liu, Z. (2025). Analysis of the Accuracy of a Body-Force Propeller Model and a Discretized Propeller Model in RANS Simulations of the Flow Around a Maneuvering Ship. *Journal of Marine Science and Engineering*, 13(4), 788. <https://doi.org/10.3390/jmse13040788>
- Choi, W. S., Min, G. S., Yun, H. C., Do, Y. U., Kim, K. M., Terziev, M., ... & Song, S. (2025). Numerical analysis on the scale effect of a free-running ship's manoeuvring characteristics. *Journal of Marine Science and Engineering*.
- Min, G., Choi, W., Yun, H., Do, Y., Kim, K., Terziev, M., ... & Song, S. (2025). Evaluation of Push-Pull manoeuvring mode for a naval ship using CFD. *Ocean Engineering*, 330, 121143.
- Celik, I. B., Ghia, U., Roache, P. J., & Freitas, C. J. (2008). Procedure for estimation and reporting of uncertainty due to discretization in CFD applications. *Journal of fluids Engineering-Transactions of the ASME*, 130(7).
- Kwon, C. S., & Yeon, S. M. (2023). CFD study to predict the effect of a passing ship on moored ships in a confined waterway. *International Journal of Naval Architecture and Ocean Engineering*, 15, 100527.
- Jung, D., & Kim, S. (2022). Computational Investigation of Seakeeping Performance of a Surfaced Submarine in Regular Waves. *Journal of Ocean Engineering and Technology*.
- Sun, S. L., Sun, J. Y., Wang, S., Li, Y. H., & Ren, H. L. (2024). Fluid–structure interaction analysis of curved wedges entering into water. *Physics of Fluids*, 36(10).

Mikkelsen, H., Shao, Y., & Walther, J. H. (2022). Numerical study of nominal wake fields of a container ship in oblique regular waves. *Applied Ocean Research*, 119, 102968.

Terziev, M., Tezdogan, T., & Incecik, A. (2019). A geosim analysis of ship resistance decomposition and scale effects with the aid of CFD. *Applied Ocean Research*, 92, 101930.

Grlj, C. G., Degiuli, N., & Martić, I. (2024). Experimental and numerical assessment of the effect of speed and loading conditions on the nominal wake of a containership. *Brodogradnja: An International Journal of Naval Architecture and Ocean Engineering for Research and Development*, 75(4), 1-34.

Mikulec, M., & Piehl, H. (2023). Verification and validation of CFD simulations with full-scale ship speed/power trial data. *Brodogradnja: An International Journal of Naval Architecture and Ocean Engineering for Research and Development*, 74(1), 41-62.